Received: 8 March 2024 | Revised: 17 April 2024 | Accepted: 21 June 2024 | Published online: 26 June 2024

RESEARCH ARTICLE

Journal of Optics and Photonics Research
2024, Vol. 1(4) 159–169
DOI: 10.47852/bonviewJOPR42022785

BON VIEW PUBLISHING

Revealing the Invisible: Imaging Through Non-radiating Subspace

Hamidreza Siampour[1,2,*] and Abolghasem Zeidaabadi Nezhad[3]

[1]*School of Mathematics and Physics, Queen's University Belfast, UK*

[2]*Department of Physics, University of Cambridge, UK*

[3]*Department of Electrical and Computer Engineering, Isfahan University of Technology, Iran*

Abstract: This paper presents a novel modification to the subspace optimization method (SOM) for solving inverse scattering problems in diverse background media. By incorporating sequential quadratic programming (SQP), a fast and accurate optimization technique, our approach aims to improve the reconstruction of dielectric objects buried in complex environments. We investigate the influence of non-radiating (NR) subspace reconstruction on imaging quality by analyzing the induced current-exterior field mapping operator's singular values. The scattering formulation of direct problems is performed through numerical methods such as coupled dipole method, finite elements-boundary integral, and electric field integral equations. Radiating and NR objective functions are defined and minimized using SQP to evaluate the effectiveness of the proposed method. Numerical experiments demonstrate significant enhancements in imaging quality, robustness, and computational efficiency compared to existing techniques. This modified SOM offers a promising avenue for precise and reliable reconstruction of electromagnetic scattering objects, with potential applications in various fields including medical imaging, remote sensing, and non-destructive evaluation.

Keywords: inverse scattering, subspace optimization method, sequential quadratic programming, non-radiating subspace, imaging

1. Introduction

Inverse problems in electromagnetics, encompassing inverse source [1, 2], inverse scattering [3–6], inverse design [7], and inverse synthesis [8] problems, have found widespread applications in various fields, including microwave imaging [9], radar tracking [10], breast cancer detecting [11], remote sensing [12], tomography [13], seismology [14], failure analysis [15], non-destructive evaluation [16], antenna design and pattern synthesis [17, 18], nanoscale optical positioning [19], and integrated quantum photonics [20–22]. Among these, electromagnetic inverse scattering focuses on detecting, locating, shape finding, and material imaging of unknown objects using scattered fields and Maxwell's equations. Different methods can be categorized into qualitative and quantitative approaches for solving inverse scattering problems. Qualitative methods, such as linear sampling [23], factorization [24], and singular sources methods [25], aim to determine the approximate shape and location of objects, providing limited information about their material properties or the surrounding medium. On the other hand, quantitative methods define an objective function related to the desired characteristics of scattering objects. These methods utilize optimization and regularization techniques to minimize the objective function and achieve more precise reconstruction of unknown objects [26]. Recent advancements in inverse scattering methods include time reversal methods based on the reciprocity of Maxwell's equations in time-invariant media [27] and subspace optimization methods (SOM) that leverage spectral analysis of the exterior mapping matrix (mapping from induced current space to exterior scattered field space) problems [28–30]. SOM focuses on minimizing the induced current residue and the scattering data mismatch, providing an alternative approach to inverse scattering problems [29].

The primary challenge in solving inverse scattering problems lies in their ill-posed nature [26], characterized by issues of non-uniqueness, non-existence, and instability of solutions [31]. The presence of non-radiating (NR) current (denote as I_{NR} or $\bar{I}^{NR}$ in discrete case) plays a significant role in the non-uniqueness aspect. The scattering field (E_{NR}) associated with the NR current vanishes outside the region of the contrast source, making it impossible to measure using receivers (as indicated by Equations (1) and (2)) [32]. To establish a relationship between the induced current ($\bar{I}^d$) from the contrast source and the internal field, previous knowledge about certain properties of the internal region is utilized to derive a current state equation. Additionally, the measurement of the external field enables the formulation of a scattering data equation, where the relation between the induced current and the scattered field is determined through the use of an exterior mapping operator $\bar{\bar{G}}_S$ (as described in Equation (2)). By combining these two equations with an appropriate reconstruction approach, it becomes possible to determine the distributions of the radiating and NR currents, thereby ensuring the uniqueness of the solution.

$$\boldsymbol{I}_{NR}(\boldsymbol{r}) = \frac{-1}{4\pi j}\left(\frac{c}{k}\right)\{\nabla \times [\nabla \times \boldsymbol{E}_{NR}(\boldsymbol{r})] - k^2 \boldsymbol{E}_{NR}(\boldsymbol{r})\} \quad (1)$$

*Corresponding author: Hamidreza Siampour, School of Mathematics and Physics, Queen's University Belfast and Department of Physics, University of Cambridge, UK. Email: h.siampour@qub.ac.uk

$$\overline{\overline{G}}_S.\bar{I}^d = \bar{E}^{sca} \xrightarrow{\overline{\overline{G}}_S.\bar{I}^{NR}=\bar{0}} \overline{\overline{G}}_S.\left(\bar{I}^d + \bar{I}^{NR}\right) = \bar{E}^{sca} \tag{2}$$

The SOM is a reconstructive approach utilized for solving inverse scattering problems by analyzing the induced current-exterior field mapping operator through singular value decomposition (SVD) [28, 29]. This method involves determining the unknown coefficients of the singular vectors that expand the induced current space by minimizing an objective function using an appropriate optimization technique, such as the contrast source inversion method.

In this paper, we propose a modification to SOM by incorporating sequential quadratic programming (SQP), a fast and accurate optimization technique [33, 34]. This is the first attempt to make use of the SQP algorithm to advance the SOM formulation for solving inverse scattering problems. This modified approach aims to address the inverse scattering problem for dielectric objects buried in diverse background mediums. Additionally, we investigate the impact of NR subspace reconstruction on the quality of imaging. This evaluation is carried out by analyzing the radiating and NR singular values of the induced current-exterior field mapping operator. To accomplish this, we define radiating and NR objective functions, constructed with and without the radiating part of the induced current, respectively.

2. Description of Inverse Scattering Problem in Different Background Mediums

2.1. Dielectric scattering objects in free-space

The inverse scattering problem under consideration involves unknown dielectric cylinders with arbitrary cross-sections positioned within a free-space background (domain D), as depicted in Figure 1. To study the scattering phenomenon, a circular array of antennas is deployed around the domain D. These antennas emit TM waves into the region and receive the corresponding scattered fields, as shown in Figure 2. To address this problem, we discretize the domain D into identical subunits and employ the coupled dipole method to formulate the direct scattering problem [28]. This formulation allows us to establish two essential equations: the current state equation (Equation (3)) and the scattering data equation (Equation (4)), respectively.

$$\boldsymbol{E}^{tot}(\boldsymbol{r}_m) = \boldsymbol{E}^{inc}(\boldsymbol{r}_m) - \sum_{n\neq m} jk_0\eta_0 g(\boldsymbol{r}_m, \boldsymbol{r}_n)\boldsymbol{I}^d(\boldsymbol{r}_n), \quad m = 1,\ 2,\ \ldots,\ N_d \tag{3}$$

$$\boldsymbol{E}^{sca}(\boldsymbol{r}_s^c) = \sum_{m=1}^{N_d} -jk_0\eta_0 g(\boldsymbol{r}_s^c, \boldsymbol{r}_m)\boldsymbol{I}^d(\boldsymbol{r}_m), \quad s = 1,\ 2,\ \ldots,\ N_r \tag{4}$$

In the given equations and descriptions: $\boldsymbol{E}^{inc}(\boldsymbol{r}_m) = E^{inc}(\boldsymbol{r}_m)\boldsymbol{z}$, $\boldsymbol{E}^{tot}(\boldsymbol{r}_m) = E^{tot}(\boldsymbol{r}_m)\boldsymbol{z}$, and $\boldsymbol{I}^d(\boldsymbol{r}_m) = I^d(\boldsymbol{r}_m)\boldsymbol{z}$, represent the incident field, the total internal field, and the induced current on the mth subunit of D, respectively (with $e^{j\omega t}$ as time dependence term being suppressed). The scattered field on the sth receiver antenna is represented by $\boldsymbol{E}^{sca}(\boldsymbol{r}_s^c) = \boldsymbol{E}^{sca}(\boldsymbol{r}_s^c)z$, and vectors $\boldsymbol{r}_m$ and $\boldsymbol{r}_s^c$ denote the position vectors of the mth subunit of D and the sth receiver antenna, respectively. In addition, N_d denotes the total number of subunits of D, N_r represents the total number of receiver antennas, $g(\boldsymbol{r}_m, \boldsymbol{r}_n) = \frac{-j}{4}H_0^{(2)}(k_0|\boldsymbol{r}_m - \boldsymbol{r}_n|)$ for $m \neq n$, is the two-dimensional free-space Green function, k_0 is the free-space wave number, and η_0 represents intrinsic impedance of free-space.

Figure 1
Unknown dielectric cylinders placed in the free-space background

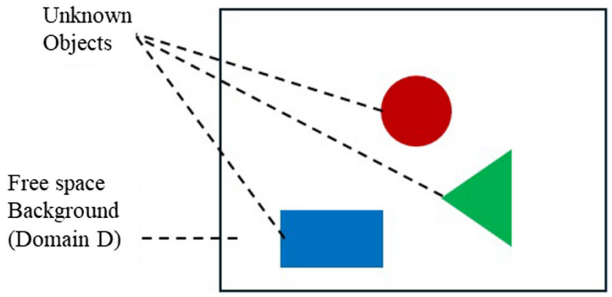

Figure 2
Setup of investigation for measurement

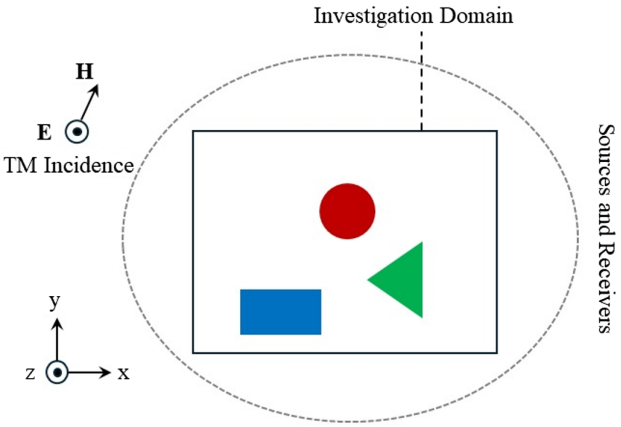

From equation $I^d(\boldsymbol{r}_m) = \xi_m E^{tot}(\boldsymbol{r}_m)$, where $\xi_m = -j(k_0/\eta_0)$ $A_m[\varepsilon_r(\boldsymbol{r}_m) - 1]$ with A_m, and $\varepsilon_r(\boldsymbol{r}_m)$ being the area and the relative permittivity of the mth subunit, respectively, the matrix forms of Equations (3) and (4) become [28]:

$$\bar{I}^d = \overline{\overline{\xi}}.\left(\bar{E}^{inc} + \overline{\overline{G_D}}.\bar{I}^d\right) \text{ Current state equation} \tag{5}$$

$$\bar{E}^{sca} = \overline{\overline{G_S}}.\bar{I}^d \text{ Scattering data equation} \tag{6}$$

where $\overline{\overline{\xi}}$ is a diagonal matrix, with N_d diagonal elements which are equal to ξ_m. The vectors $\bar{I}^d$ and $\bar{E}^{inc}$ are N_d dimensional and represent the induced currents and incident fields on the N_d subunits of D, respectively, and are given by $\bar{I}^d = \left[I^d(\boldsymbol{r}_1), I^d(\boldsymbol{r}_2), \ldots,\ I^d\left(\boldsymbol{r}_{N_d}\right)\right]^T$ and $\bar{E}^{inc} = \left[E^{inc}(\boldsymbol{r}_1), E^{inc}(\boldsymbol{r}_2), \ldots,\ E^{inc}\left(\boldsymbol{r}_{N_d}\right)\right]^T$. The elements of the interior mapping matrix $\overline{\overline{G_D}}$ are given by $\overline{\overline{G_D}}(m,n) = -jk_0\eta_0 g(\boldsymbol{r}_m, \boldsymbol{r}_n)$. Furthermore, the scattered field is $\bar{E}^{sca} = \left[E^{sca}(\boldsymbol{r}_1^c), E^{sca}(\boldsymbol{r}_2^c), \ldots,\ E^{sca}\left(\boldsymbol{r}_{N_r}^c\right)\right]^T$, and the exterior mapping matrix $\overline{\overline{G_S}}$, with dimensions $N_r \times N_d$, is given by $\overline{\overline{G_S}}(s,m) = -jk_0\eta_0 g(\boldsymbol{r}_s^c, \boldsymbol{r}_m)$.

2.1.1. Spectral analysis of $\overline{\overline{G_S}}$ using SVD

From SVD analysis, the exterior mapping matrix $\overline{\overline{G_S}}$, becomes $\overline{\overline{G_S}} = \sum_m \bar{u}_m\sigma_m\bar{v}_m^*$, with $\overline{\overline{G_S}}.\bar{v}_m = \sigma_m\bar{u}_m$, $m = 1,\ 2,\ \ldots,\ N_d$,

where σ_m are singular values of $\overline{\overline{G_S}}$, $\bar{v}_m$ are N_d dimensional basis vectors in the induced current space, and $\bar{u}_m$ are N_r dimensional basis vectors in the scattering data space. Also, * denotes transpose-conjugate operator. There are L_0 numbers of non-vanishing and $N_d - L_0$ vanishing singular values with non-increasing order as

$$\sigma_1 \geq \sigma_2 \geq \ldots \geq \sigma_{L_0} > \sigma_{L_0+1} = \sigma_{L_0+2} \ldots = \sigma_{N_d} = 0 \quad (7)$$

By using vanishing and non-vanishing singular values and the corresponding singular vectors in the induced current space, the radiating and NR subspaces of the induced current can be expressed as [28]:

$$\bar{I}^R = \sum_{j=1}^{L_0} \frac{\bar{u}_j^* . \bar{E}^{sca}}{\sigma_j} \bar{v}_j \text{ Radiating subspace} \quad (8)$$

$$\bar{I}^{NR} = \sum_{j=1}^{N_d - L_0} \bar{\alpha}_j^{NR} \bar{v}_{j+L} = \bar{V}^{NR} . \bar{\alpha}^{NR} \text{ NR subspace} \quad (9)$$

in which $\bar{\alpha}_j^{NR}$ are NR coefficients and will be determined by the least square procedure as explained in Section 2.2.2. From Equations (8) and (9), the total induced current ($\bar{I}^d$) becomes

$$\bar{I}^d = \bar{I}^R + \bar{I}^{NR} \quad (10)$$

In Equation (10), $\bar{I}^R$ represents the radi ating subspace, i.e., $\overline{\overline{G_S}} . \bar{I}^R = \bar{E}^{sca}$, and $\bar{I}^{NR}$ denotes the NR subspace, i.e., $\overline{\overline{G_S}} . \bar{I}^{NR} = 0$.

2.1.2. Determination of NR coefficients

From Equations (5), (9), and (10), one can obtain the vector $\bar{\alpha}^{NR}$ with dimension of $N_d - L_0$ and consists of NR coefficients $\bar{\alpha}_j^{NR}$ obtained from

$$\overline{\overline{A}} . \bar{\alpha}^{NR} = \bar{B} \quad (11)$$

where $\overline{\overline{A}} = \left[\overline{\overline{V}}^{NR} - \bar{\bar{\xi}} . \left(\overline{\overline{G_D}} . \overline{\overline{V}}^{NR} \right) \right]$ and $\bar{B} = \left[\bar{\bar{\xi}} . \left(\bar{E}^{inc} + \overline{\overline{G_D}} . \bar{I}^R \right) - \bar{I}^R \right]$. From the least square procedure, Equation (11) gives

$$\left(\overline{\overline{A}}^* . \overline{\overline{A}} \right) . \bar{\alpha}^{NR} = \overline{\overline{A}}^* . \bar{B} \Rightarrow \bar{\alpha}^{NR} = \left(\overline{\overline{A}}^* . \overline{\overline{A}} \right)^{-1} . \left(\overline{\overline{A}}^* . \bar{B} \right) \quad (12)$$

2.1.3. Objective function

The residue of the scattering data and the mismatch of the induced current, give Equations (13) and (14), respectively.

$$\Delta^{dat} = \left\| \overline{\overline{G_s}} . \overline{\overline{V}}^{NR} . \bar{\alpha}^{NR} + \overline{\overline{G_s}} . \bar{I}^R - \bar{E}^{sca} \right\|^2 \quad (13)$$

$$\Delta^{sta} = \left\| \overline{\overline{A}} . \bar{\alpha}^{NR} - \bar{B} \right\|^2 \quad (14)$$

which $\|.\|$ denotes the Euclidean length. The objective function for inverse scattering problem can be defined as

$$f\left(\bar{\bar{\xi}} \right) = \sum_{p=1}^{N_t} \left(\Delta_p^{dat} / \left\| \bar{E}_p^{sca} \right\|^2 + \Delta_p^{sta} / \left\| \bar{I}_p^R \right\|^2 \right)^2 \quad (15)$$

In Equation (15), the subscripts p and N_t denote dependency on the transmitter incidence and the number of transmitters, respectively. The unknowns of the objective function are the diagonal elements of matrix $\bar{\bar{\xi}}$, in which the unknown permittivity of dielectric cylinders is represented, and will be obtained using SQP algorithm for optimization, enabling fast internal linear algebra for solving quadratic programs [34].

Radiating objective function can be defined from Equations (13), (14), and (15), but without NR subspace of the current such as:

$$f^{Rad}\left(\bar{\bar{\xi}} \right) = \sum_{p=1}^{N_t} \left(\frac{\left\| \overline{\overline{G_s}} . \bar{I}_p^R - \bar{E}_p^{sca} \right\|^2}{\left\| \bar{E}_p^{sca} \right\|^2} + \frac{\left\| \bar{B}_p \right\|^2}{\left\| \bar{I}_p^R \right\|^2} \right)^2 \quad (16)$$

where the subscript p denotes dependence on the transmitter incidence. By comparing the imaging results of the two objective functions from Equations (15) and (16), the effect of NR current on the reconstructed object can be determined.

2.2. Buried dielectric objects

2.2.1. Buried objects in inhomogeneous medium

Considering an inhomogeneous medium containing buried dielectric cylinders with arbitrary cross-sections, as depicted in Figure 3, and an equispaced array of antennas surrounding the inhomogeneous background domain D. The antennas are used to emit TM waves into the medium and receive the corresponding scattered fields.

The dielectric constant of the inhomogeneous background (domain D) and the buried dielectric cylinders are $\varepsilon_{rb}(\boldsymbol{r})$ and $\varepsilon_r(\boldsymbol{r})$, respectively. The background field $E_b(\boldsymbol{r})$ and the total field $E(\boldsymbol{r})$ satisfy the Helmholtz equation in D [35, 36]:

$$[\nabla^2 + k_0^2 \varepsilon_{rb}(\boldsymbol{r})](E(\boldsymbol{r}) - E_b(\boldsymbol{r})) = -k_0^2 [\varepsilon_{\boldsymbol{r}}(\boldsymbol{r}) - \varepsilon_{rb}(\boldsymbol{r})] E(\boldsymbol{r}) \quad (17)$$

From right side of Equation (17), the induced current on the unknown objects located in domain D is $I^{cur}(\boldsymbol{r}) = \frac{-I^d(\boldsymbol{r})}{j\omega\mu}$, in which $I^d(\boldsymbol{r}) = k_0^2 [\varepsilon_r(\boldsymbol{r}) - \varepsilon_{rb}(\boldsymbol{r})] E(\boldsymbol{r})$, ω is the angular frequency of the incident wave, and μ is the permeability of the space. Because of simplification, we use $I^d(\boldsymbol{r})$, instead of $I^{cur}(\boldsymbol{r})$ for induced current in the following. The induced current $I^d(\boldsymbol{r})$ reradiates the scattered field $E^{sca}(\boldsymbol{r}) = (E(\boldsymbol{r}) - E_b(\boldsymbol{r}))$.

To derive the variational form of Equation (17), we multiply both sides by a weighting function $W(r)$, in order to enforce it on an average and therefore weaker sense, and integrate over D [35] as

$$\iint_D (\nabla W(\boldsymbol{r}) . \nabla E^{sca}(\boldsymbol{r}) - k_0^2 \varepsilon_{rb}(\boldsymbol{r}) W(\boldsymbol{r}) E^{sca}(\boldsymbol{r})) ds = \iint_D W(\boldsymbol{r}) I^d(\boldsymbol{r}) ds + \oint_C W(\boldsymbol{r}) \frac{\partial E^{sca}(r)}{\partial n} dC. \quad (18)$$

where $\frac{\partial}{\partial n}$ represents the derivative along the normal direction of boundary C.

In the exterior region, the scattered field can be obtained from boundary integral equation as [35, 36]

$$E^{sca}(\boldsymbol{r}) = \oint_C \left\{ -G(\boldsymbol{r}, \boldsymbol{r}') \frac{\partial E^{sca}(\boldsymbol{r}')}{\partial n'} + E^{sca}(\boldsymbol{r}') \frac{\partial G(\boldsymbol{r}, \boldsymbol{r}')}{\partial n'} \right\} dC' \quad (19)$$

where $\boldsymbol{r}$ represents the position vector of receivers. The Equation (19) at the boundary C, i.e., ($\boldsymbol{r} \varepsilon C$), becomes the following boundary condition, known as Kirchhoff's boundary integral [37]:

Figure 3
Unknown dielectric cylinders buried in an inhomogeneous background

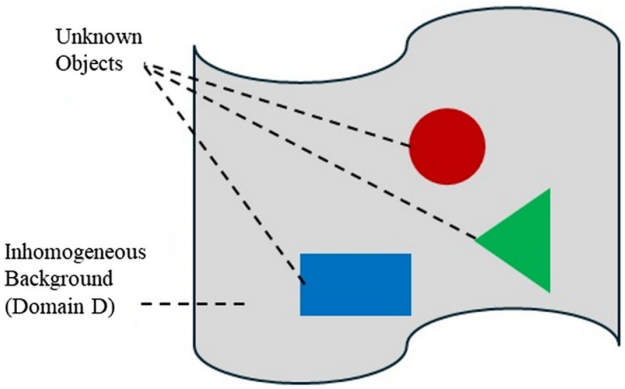

$$E^{sca}(\boldsymbol{r})|_{r\varepsilon C} = \oint_C \left\{ -G(\boldsymbol{r},\boldsymbol{r}')\frac{\partial E^{sca}(\boldsymbol{r}')}{\partial n'} + E^{sca}(\boldsymbol{r}')\frac{\partial G(\boldsymbol{r},\boldsymbol{r}')}{\partial n'} \right\} dC' \tag{20}$$

The interior scattered field $E^{sca}(\boldsymbol{r})$ can be expanded at the nodes of D by using the basis functions $B_n(\boldsymbol{r})$ which are equal to weighting function $W(\boldsymbol{r})$ (Galerkin FEM) as [35]:

$$E^{sca}(r) \simeq \sum_{n=1}^{N_{int}} E_n^{int} B_n(r) + \sum_{n=1}^{N_{bou}} E_n^{bou} B_n(r) \tag{21}$$

where E_n^{int} and E_n^{bou} represent the value of scattered field at the interior and boundary nodes, respectively, and N_{int} and N_{bou} denote the number of interior and boundary nodes, respectively. Similarly, the induced current $I^d(\boldsymbol{r})$ can be expanded. By using the projection of $B_n(\boldsymbol{r})$ onto the boundary, the scattered field at the boundary C given by [35]:

$$E^{sca}(\boldsymbol{r})|_{\boldsymbol{r}\varepsilon C} \simeq \sum_{n=1}^{N_{bou}} E_n^{bou} B_n(\boldsymbol{r})|_{r\varepsilon C} \tag{22}$$

By using N_d number of rectangular subunits (cells) for grid mesh, the quadrilateral elements of the node-based bilinear basis functions are such as [36]:

$$N_1^e = \frac{1}{A^e} * \left(x_c^e + \frac{h_x^e}{2} - x \right) * \left(y_c^e + \frac{h_y^e}{2} - y \right) \tag{23}$$

$$N_2^e = \frac{1}{A^e} * \left(-x_c^e + \frac{h_x^e}{2} + x \right) * \left(y_c^e + \frac{h_y^e}{2} - y \right) \tag{24}$$

$$N_3^e = \frac{1}{A^e} * \left(-x_c^e + \frac{h_x^e}{2} + x \right) * \left(-y_c^e + \frac{h_y^e}{2} + y \right) \tag{25}$$

$$N_4^e = \frac{1}{A^e} * \left(x_c^e + \frac{h_x^e}{2} - x \right) * \left(-y_c^e + \frac{h_y^e}{2} + y \right) \tag{26}$$

where A^e denotes the area of the subunit, and x_c^e, y_c^e, h_x^e, and h_y^e are shown in Figure 4.

In the Equation (20), the equivalent boundary current $I^{bou}(\boldsymbol{r}') = \frac{\partial E^{sca}(\boldsymbol{r}')}{\partial n'}$ can be expanded by using the piecewise constant basis functions $\tilde{B}_n(\boldsymbol{r}')$ as follows [35]:

Figure 4
Rectangular subunit and the corresponding nodes of the element

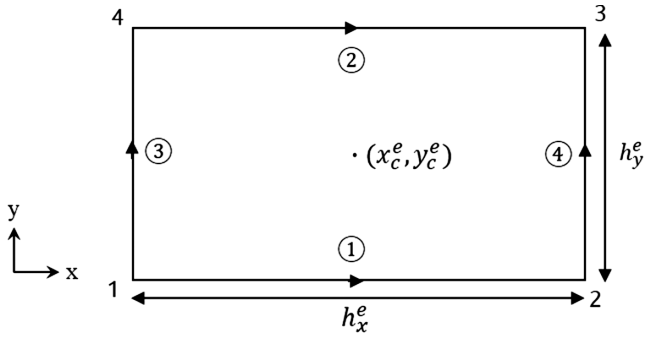

$$I^{bou}(r') \simeq \sum_{n=1}^{N_{bou}} I_n^{bou} \tilde{B}_n(r') \tag{27}$$

From the use of above Galerkin FEM formulation, and using the corresponding expansion equations in Equation (18), the following matrix representation can be obtained:

$$\begin{bmatrix} \overline{\overline{X}}^{int} & \overline{\overline{X}}^{cros,A} \\ \overline{\overline{X}}^{cros,B} & \overline{\overline{X}}^{bou} \end{bmatrix} \cdot \begin{bmatrix} \overline{E}_{int}^{sca} \\ \overline{E}_{bou}^{sca} \end{bmatrix} = \begin{bmatrix} \overline{\overline{Z}}^{int} & \overline{\overline{Z}}^{cros,A} \\ \overline{\overline{Z}}^{cros,B} & \overline{\overline{Z}}^{bou} \end{bmatrix} . \overline{I}^d + \begin{bmatrix} \overline{0} \\ \overline{\overline{Y}} . \overline{I}^{bou} \end{bmatrix} \tag{28}$$

where $\overline{\overline{X}}_{mn} = \iint_D (\nabla B_m . \nabla B_n - k_0^2 \varepsilon_{rb}(\boldsymbol{r}) B_m B_n) ds$ represents the common form of $\overline{\overline{X}}^{int}$, $\overline{\overline{X}}^{cros,B}$, and $\overline{\overline{X}}^{bou}$, and $\overline{\overline{Z}}_{mn} = \iint_D B_m B_n ds$ represents $\overline{\overline{Z}}^{int}$, $\overline{\overline{Z}}^{cros,A}$, $\overline{\overline{Z}}^{cros,B}$, and $\overline{\overline{Z}}^{bou}$. Also the elements of $\overline{\overline{Y}}$ are given by $\overline{\overline{Y}}_{mn} = \oint_C B_m \tilde{B}_n dC$.

By using the piecewise constant expansion for boundary field $E^{sca}(\boldsymbol{r}')$ and boundary current $I^{bou}(\boldsymbol{r}')$, the Equation (20) yields [36]:

$$\begin{aligned} &E^{sca}(\boldsymbol{r})|_{\boldsymbol{r}\varepsilon C} \\ &+ \sum\nolimits_{n=1}^{N_{bou}} \left\{ I_n^{bou} \int_{C_n} G(\boldsymbol{r},\boldsymbol{r}') dC' - \left(\frac{E_n^{bou} + E_{n+1}^{bou}}{2} \right) \int_{C_n} \frac{\partial G(\boldsymbol{r},\boldsymbol{r}')}{\partial n'} dC' \right\} \\ &= R(\boldsymbol{r})|_{r\varepsilon C}, \end{aligned} \tag{29}$$

where C_n denotes the nth segment around the boundary C, and $E_{N_{bou}+1}^{bou} = E_1^{bou}$, and $R(\boldsymbol{r})$ is the residual. Applying the weighted residual method, i.e., $\oint_C W(\boldsymbol{r}) R(\boldsymbol{r}) dC' = 0$, and implying point matching, the Equation (29) yields [36]

$$\begin{aligned} &\frac{E_m^{bou} + E_{m+1}^{bou}}{2} + \sum\nolimits_{n=1}^{N_{bou}} \left\{ I_n^{bou}\, G_{Mmn} - \left(\frac{E_n^{bou} + E_{n+1}^{bou}}{2} \right) G_{\nabla mn} \right\} \\ &= 0, \quad m = 1, 2, \ldots, N_{bou} \end{aligned} \tag{30}$$

where $G_{Mmn} = \int_{C_n} G(|\boldsymbol{r}_m - \boldsymbol{r}'|) dC'$, and $G_{\nabla mn} = \int_{C_n} \frac{\partial G(|\boldsymbol{r}_m - \boldsymbol{r}'|)}{\partial n'} dC'$.

Using $|\boldsymbol{r}_m - \boldsymbol{r}'| \simeq R_{mn} = \sqrt{|\boldsymbol{r}_m|^2 + |\boldsymbol{r}_n|^2 - 2|\boldsymbol{r}_m||\boldsymbol{r}_n|\cos(\varphi_m - \varphi_n)}$, in which $|\boldsymbol{r}_n| \angle \varphi_n$ denotes the position vector of center of boundary segment C_n, and based on the helpful circular approximation equations represented in reference [36], we obtain the following approximate representations for G_{Mmn} and $G_{\nabla mn}$:

$$G_{M\,mn} = \begin{cases} -\frac{j|\boldsymbol{r}_n|\Delta\varphi_n}{4}\left\{1 - j\frac{2}{\pi}\left[\ln\left(\frac{\gamma k_0|\boldsymbol{r}_n|\Delta\varphi_n}{4}\right) - 1\right]\right\}; & m = n \\ -\frac{j|\boldsymbol{r}_n|\Delta\varphi_n}{4}H_0^{(2)}(k_0R_{mn}); & m \neq n \end{cases} \tag{31}$$

$$G_{\nabla\,mn} = \begin{cases} \frac{1}{2} + \frac{jk_0|\boldsymbol{r}_n|}{4}\left[k_0|\boldsymbol{r}_n|\left(\frac{\Delta\varphi_n}{2} - \sin\left(\frac{\Delta\varphi_n}{2}\right)\right) + \frac{j\Delta\varphi_n}{\pi k_0|\boldsymbol{r}_n|}\right]; & m = n \\ \frac{jk_0R_{mn}\Delta\varphi_n}{8}H_1^{(2)}(k_0R_{mn}); & m \neq n \end{cases} \tag{32}$$

where $\Delta\varphi_n$ is the phase difference between two nodes of the boundary segment C_n, and $\gamma = 1.781072418$ is Euler's constant.

The linearly independent equations in Equation (30) can be expressed in the following matrix form:

$$\overline{\overline{G}}_L\bar{E}^{sca}_{bou} + \overline{\overline{G}}_M\bar{I}^{bou} = 0 \tag{33}$$

where $\overline{\overline{G}}_L$ is given by

$$\overline{\overline{G}}_L = 0.5 * \left(\bar{I}_{N_{bou}\times N_{bou}} - \overline{\overline{G}}_\nabla\right) * \overline{\overline{O}}_{\nabla N_{bou}\times N_{bou}} \tag{34}$$

with $\overline{\overline{O}}_\nabla = \begin{bmatrix} 1 & 1 & & 0 \\ & \ddots & \ddots & \\ & & & 1 \\ & 0 & & 1 \\ 1 & & & \end{bmatrix}$. The elements of $\overline{\overline{G}}_M$ and $\overline{\overline{G}}_\nabla$ are represented in Equations (31) and (32).

From use of Equations (28) and (33), the following matrix equation can be obtained:

$$\begin{bmatrix} \overline{\overline{X}}^{int} & \overline{\overline{X}}^{cros,\ A} \\ \overline{\overline{X}}^{cros,\ B} & \overline{\overline{X}}^{bou} + \overline{\overline{Y}}.\overline{\overline{G}}_M{}^{-1}.\overline{\overline{G}}_L \end{bmatrix}.\begin{bmatrix} \bar{E}^{sca}_{int} \\ \bar{E}^{sca}_{bou} \end{bmatrix} = \begin{bmatrix} \overline{\overline{Z}}^{int} & \overline{\overline{Z}}^{cros,\ A} \\ \overline{\overline{Z}}^{cros,\ B} & \overline{\overline{Z}}^{bou} \end{bmatrix}.\bar{I}^d \tag{35}$$

From Equation (35), we have the following expression for interior scattered field-induced current equation:

$$\begin{bmatrix} \bar{E}^{sca}_{int} \\ \bar{E}^{sca}_{bou} \end{bmatrix} = \overline{\overline{G_D}}.\bar{I}^d \tag{36}$$

with $\overline{\overline{G_D}} = \begin{bmatrix} \overline{\overline{X}}^{int} & \overline{\overline{X}}^{cros,A} \\ \overline{\overline{X}}^{cros,B} & \overline{\overline{X}}^{bou} + \overline{\overline{Y}}.\overline{\overline{G}}_M{}^{-1}.\overline{\overline{G}}_L \end{bmatrix}^{-1}.\begin{bmatrix} \overline{\overline{Z}}^{int} & \overline{\overline{Z}}^{cros,A} \\ \overline{\overline{Z}}^{cros,\ B} & \overline{\overline{Z}}^{bou} \end{bmatrix}$.

Matrix $\overline{\overline{G_D}}$ is the interior mapping operator from the induced current to the internal scattered field.

Multiplying the two sides of the Equation (36) with $\overline{\overline{P}} = \left[\overline{\overline{O}}_{N_{bou}\times N_{int}}, \bar{I}_{N_{bou}\times N_{bou}}\right]$, where $\bar{I}$ and $\overline{\overline{O}}$ denote identity and zero matrices, respectively [35], we obtain the following equation that is known as discrete boundary scattered field equation:

$$\bar{E}^{sca}_{bou} = \overline{\overline{P}}.\overline{\overline{G_D}}.\bar{I}^d \tag{37}$$

Also, the boundary integral Equation (19) can be discretized as Equation (38):

$$\bar{E}^{sca} = -\overline{\overline{G}}_{L_s}\bar{E}^{sca}_{bou} - \overline{\overline{G}}_{M_s}\bar{I}^{bou} \tag{38}$$

with $\overline{\overline{G}}_{M_s} = -\frac{j|\boldsymbol{r}_n|\Delta\varphi_n}{4}H_0^{(2)}(k_0R_{qn})$, and $\overline{\overline{G}}_{L_s} = 0.5 * \left(-\overline{\overline{G}}_{\nabla_s}\right) * \overline{\overline{O}}_{\nabla N_{bou}\times N_{bou}}$,

where $R_{qn} = \sqrt{|\boldsymbol{r}_q|^2 + |\boldsymbol{r}_n|^2 - 2|\boldsymbol{r}_q||\boldsymbol{r}_n|\cos(\varphi_q - \varphi_n)}$,

and $\overline{\overline{G}}_{\nabla_s} = \frac{jk_0R_{qn}\Delta\varphi_n}{8}H_1^{(2)}(k_0R_{qn})$. Also, $|\boldsymbol{r}_q|\angle\varphi_q$ denotes the position vector of qth receiver, and $|\boldsymbol{r}_n|\angle\varphi_n$ denotes the position vector of the center of the boundary segment C_n.

From Equations (33), (37), and (38), the data scattering equation can be obtained such as follows [37]:

$$\bar{E}^{sca} = \overline{\overline{G_S}}.\bar{I}^d \tag{39}$$

in which $\overline{\overline{G_s}} = \left(-\overline{\overline{G}}_{L_s} + \overline{\overline{G}}_{M_s}.\overline{\overline{G}}_M{}^{-1}.\overline{\overline{G}}_L\right).\overline{\overline{P}}.\overline{\overline{G_D}}.\bar{I}^d$.

Matrix $\overline{\overline{G_s}}$ is a $N_s \times (N_{int} + N_{bou})$ dimensional matrix known as exterior mapping matrix, in which N_s is the number of receivers. The induced current $\bar{I}^d = k_0^2[\varepsilon_r(\boldsymbol{r}) - \varepsilon_{rb}(\boldsymbol{r})]\left(\bar{E}^{sca} + \bar{E}_b\right)$, combined with Equation (39), gives the following form for the current state equation

$$\bar{I}^d = \bar{\bar{\xi}}.\left(\bar{E}_b + \overline{\overline{D}}_D.\bar{I}^d\right) \tag{40}$$

where $\bar{E}_b$ is a $(N_{int} + N_{bou}) \times 1$ vector, representing the background (or incident) field at the domain nodes. Also, diagonal matrix $\bar{\bar{\xi}}$, with $(N_{int} + N_{bou})$ diagonal elements $k_0^2[\varepsilon_r(\boldsymbol{r}) - \varepsilon_{rb}(\boldsymbol{r})]$, represents the unknown objects' permittivity at the domain nodes, in the inverse scattering problem. Notice that $\bar{I}^d$ represents the induced current only on the objects not on the inhomogeneous background.

2.2.2. Buried objects under stratified media

In this scenario, we consider a stratified media where dielectric cylinders with arbitrary cross-sections are buried within domain D, as shown in Figure 5. An equispaced array of antennas is deployed, which emits TM waves from the upper region into the domain and receives the corresponding scattered fields.

The electric field inside the domain D (internal field) and the total scattered field in the upper space ($z > z_n$) can be obtained by using EFIE as presented in Cui et al. [38]. From EFIE formulation, the current state and the scattering data equations can be expressed as

$$\bar{E}^{tot} = \bar{E}^{inc} + \overline{\overline{G_D}}.\bar{I}^d \tag{41}$$

Figure 5
Unknown dielectric cylinders buried in the bottom layer of a stratified media

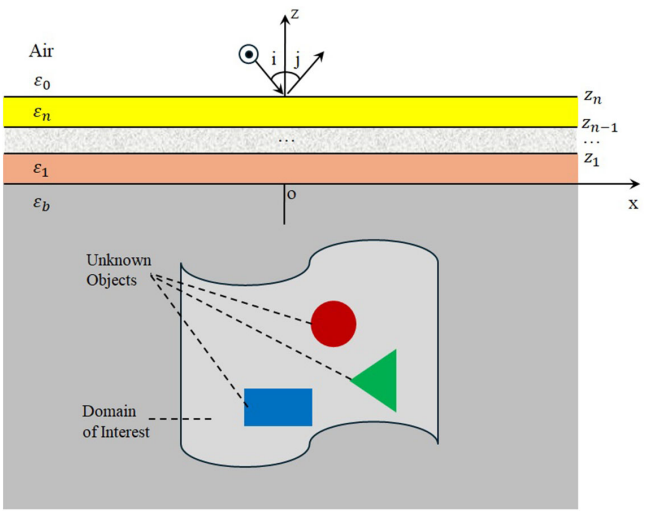

Figure 6
(a) Relative permittivity profile of the exact dielectric cylinders. (b) Reconstructed results using SQP-SOM with NR current consideration (frequency of incidence: 400 MHz). (c) Reconstructed results without considering the NR part of the current

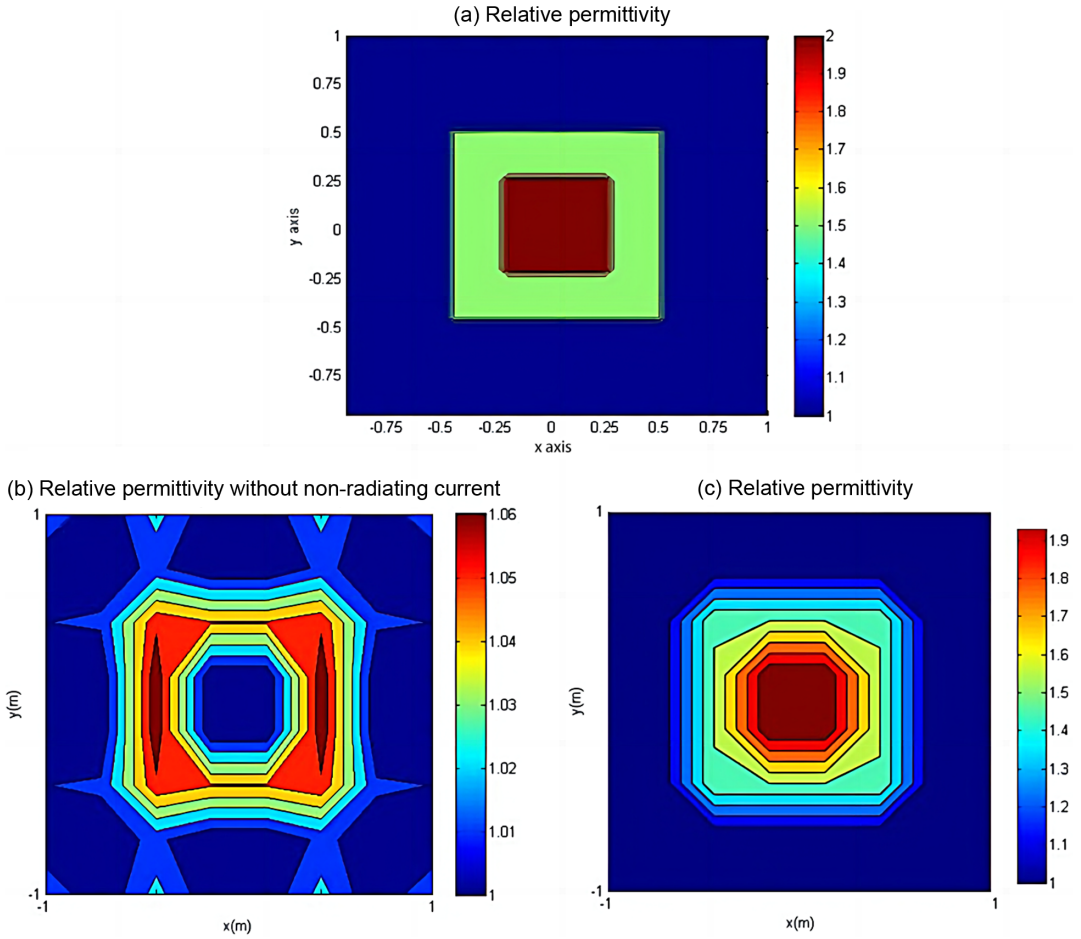

$$\overline{E}^{sca} = \overline{\overline{G_S}}.\overline{I}^{d} \tag{42}$$

where $\overline{E}^{tot}(m), \overline{E}^{inc}(m)$, and $\overline{I}^{d}(m) = j(k_0/\eta_0)A_m[\varepsilon_r(\boldsymbol{r}_m) - \varepsilon_b]$. $\overline{E}^{tot}$ represent the total internal field, the incident field, and the induced current on the N_d subunits of D, respectively. Matrix $\overline{\overline{G_D}}$ denotes internal mapping operator, and given by $\overline{\overline{G_D}}(m,n) = (k_0\eta_0/4\pi)\int_{-\infty}^{\infty} \beta_b^{-1}\left[e^{-j\beta_b|z_m - z_n|} + r^{+}(k_0,\xi)e^{j\beta_b|z_m+z_n|}\right]e^{j\xi(x_m - x_n)}d\xi$, which $\beta_b = \sqrt{k_0^2\varepsilon_b^2 - \xi^2}$, and $(x_m,\ z_m)$ represents the position of the mth subunit of D [38], and r^{+} is reflection coefficient from background ε_b to air and can be found in Kong [37]. Also, $\overline{E}^{sca} = \overline{E}^{sca}_{tot} - \overline{E}^{sca}_{1}$, where $\overline{E}^{sca}_{tot}$ is the total scattered field vector, and $\overline{E}^{sca}_{1}$ is the reflected field vector by the stratified medium and can be calculated from Cui et al. [38]. Matrix $\overline{\overline{G_S}}$, denotes exterior mapping operator, and given by $\overline{\overline{G_S}}(s,m) = \int_{-\infty}^{\infty} \beta_b^{-1}t^{+}(k_0,\xi)e^{-j(\beta_a z_s^c - \beta_b z_m)}e^{j\xi(x_s^c - x_m)}d\xi$, which $\beta_a = \sqrt{k_0^2 - \xi^2}$, and $(x_s^c,\ z_s^c)$ represents the position of the sth receiver antenna [38]. Also, t^{+} is transmission coefficient from background ε_b to air and can be found in Kong [37]. To calculate the elements of $\overline{\overline{G_D}}$, and $\overline{\overline{G_S}}$, one should implement a proper numerical method to solve the concerned integrals.

3. Inverse Scattering by SQP-SOM

By performing SVD analysis of the exterior mapping matrix $(\overline{\overline{G_s}})$, as explained in Section 2.1.1, and determining the NR coefficients as described in Section 2.1.2, we can construct the objective function and radiating objective function. These functions are based on the relative residue of the scattering data and the relative mismatch of the induced current, considering or excluding the NR current, as discussed in Section 2.1.3.

Given the nonlinear [39] and quadratic nature of the objective functions, the SQP algorithm is well-suited for solving the inverse scattering problem. The SQP algorithm provides performance parameters such as efficiency, accuracy, and the percentage of successful solutions [34, 40]. It involves updating the Hessian matrix, solving quadratic programming subproblems, performing line searches, and minimizing the merit function. The Hessian matrix represents the second-order partial derivatives of the

Figure 7

Exact relative permittivity profile of the buried objects in the inhomogeneous medium: (a) 2D image; (b) 3D plot. Reconstructed results based on non-radiating (NR) current using the SQP-SOM method: (c) 3D plot of the reconstructed relative permittivity; (d) 2D image of the reconstructed relative permittivity

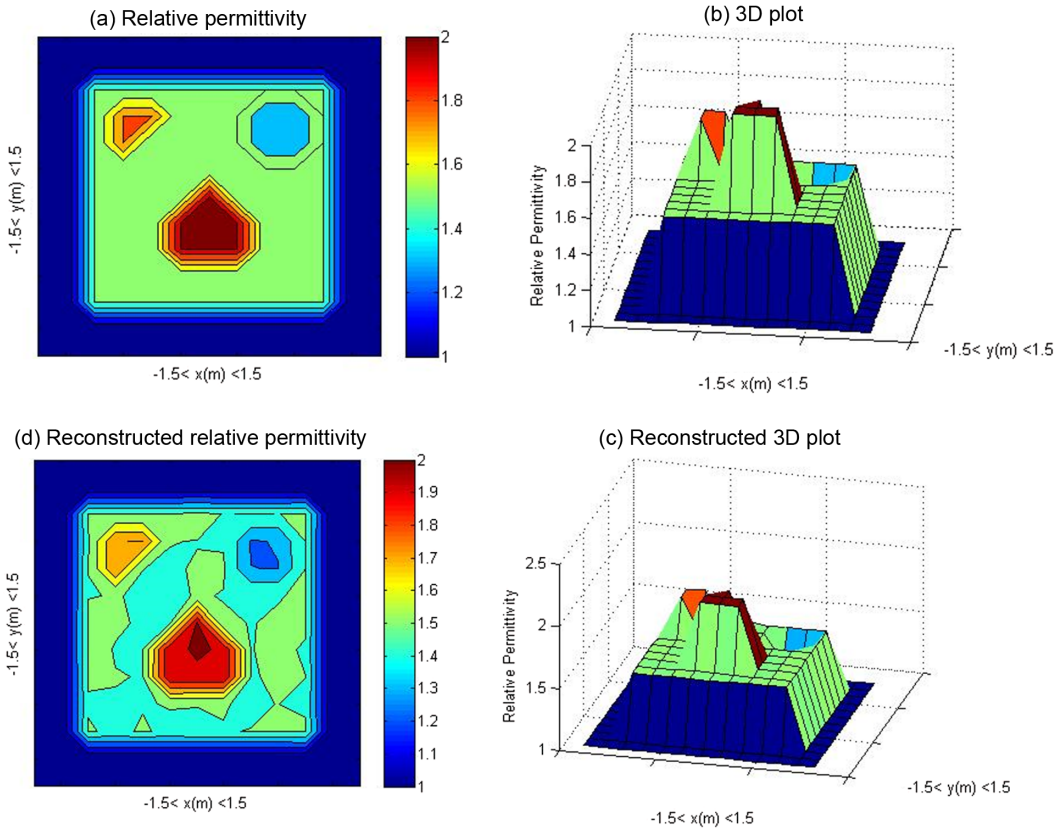

objective function and characterizes the local curvature of the objective function with respect to the variables involved. The merit function, on the other hand, measures the agreement between the observed data and the fitted model, determining the best-fit parameters by minimizing this function [41].

By minimizing the obtained objective functions using the SQP algorithm, we can reconstruct the unknown scattering objects. To enhance the resolution of the material imaging results, a frequency hopping procedure can be employed by increasing the frequency of the incident waves.

4. Numerical Results

4.1. Free-space

In the case of free-space, we consider a square domain with dimensions 2 m × 2 m as the free-space region. Within this domain, there is a dielectric cylinder in the form of a square with dimensions 0.5 m × 0.5 m and a relative permittivity of 2. Additionally, there is a dielectric layer with a thickness of 0.25 m and a relative permittivity of 1.5, as depicted in Figure 6(a). We implemented our own codes in MATLAB and utilized its optimization and visualization toolboxes for conducting this simulation. The reconstructed results, obtained with and without considering the NR part of the currents, are presented in Figure 6 (b)–(c), respectively. From the figure, it is evident that the material imaging of the relative permittivity using NR current reconstruction is accurate, while the reconstruction without considering the NR part is not satisfactory. However, the results for detecting, shape finding, and locating the objects are acceptable in both cases.

4.2. Inhomogeneous medium

In this section, we investigate the inverse scattering problem in an inhomogeneous medium containing three dielectric cylinders with different cross-sections, as depicted in Figure 7. Our experimental setup consists of 10 transmitting and receiving antennas, and we employ a grid mesh with 124 subunits. In Figure 7(a), the square region with a relative permittivity of 1.5 represents the inhomogeneous background medium. The bottom object, characterized by a relative permittivity of 2, corresponds to object 1. The two objects located at the top left and top right regions, with relative permittivities of 1.8 and 1.3, respectively, represent objects 2 and 3. The reconstructed results with and without considering the NR part of the currents are presented in Figure 7 (c)–(d) and Figure 8, respectively. It is evident from the comparison between these figures that the NR current reconstruction leads to accurate locating, shaping, and material imaging results. On the other hand, the reconstructions without considering the NR current produce unsatisfactory results.

4.3. Stratified media

Considering three dielectric cylinders with arbitrary cross-sections buried under a stratified media with two layers, we assume a semicircular array of antennas with 10 elements for

Figure 8
Reconstructed results with the radiating objective function: (a) 3D plot of the reconstructed relative permittivity, (b) 2D image of the reconstructed relative permittivity

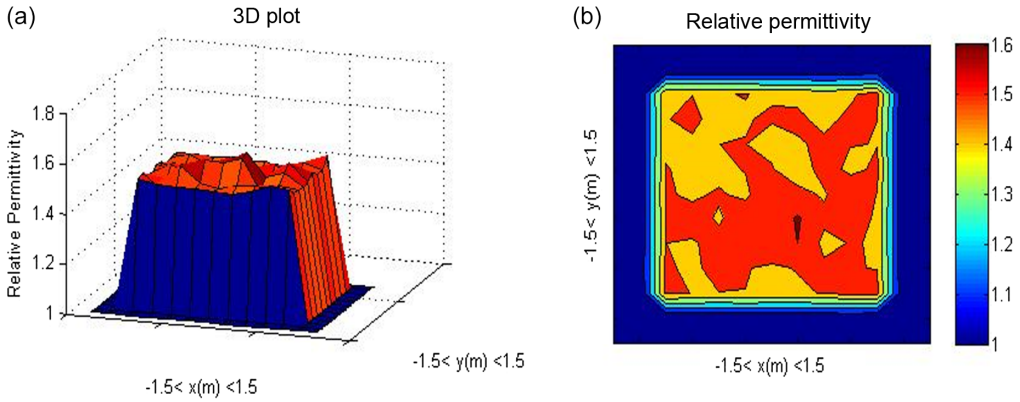

transmitting and receiving TM waves, as illustrated in Figure 9(a). The relative permittivity of the first layer (ε_1) is 1.5, and ε_b is equal to 2. In Figure 9(b), the square domain with a relative permittivity of 2 represents the homogeneous background of the buried objects. The bottom rectangular cylinder in the domain with a relative permittivity of 1.8 denotes object 1, and the two square cylinders on top of object 1, on the left and right sides with relative permittivities of 2.2 and 2.4, represent objects 2 and 3, respectively. Figure 9(c) shows the corresponding 3-D plot of the relative permittivity profile.

Figure 9
(a) Setup of investigation for single-side incidence. Exact relative permittivities of the buried objects: (b) Relative permittivity of the exact buried objects; (c) 3-D plot of the exact relative permittivity

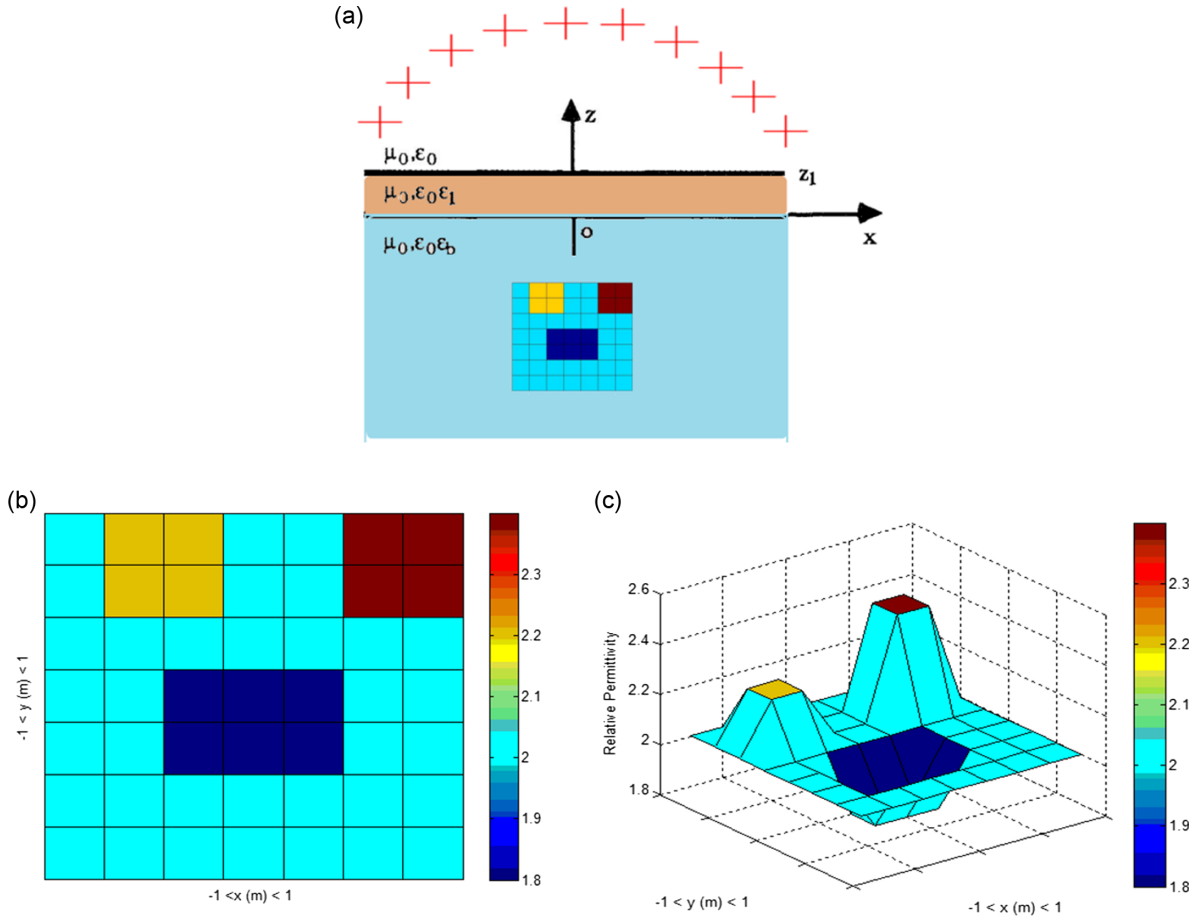

Figure 10

Reconstructed results based on NR current using SQP-SOM with the frequency hopping approach. (a) $f = 300\ MHz$; (b) $f = 400$; (c) $f = 500\ MHz$; and (d) $f = 600\ MHz$

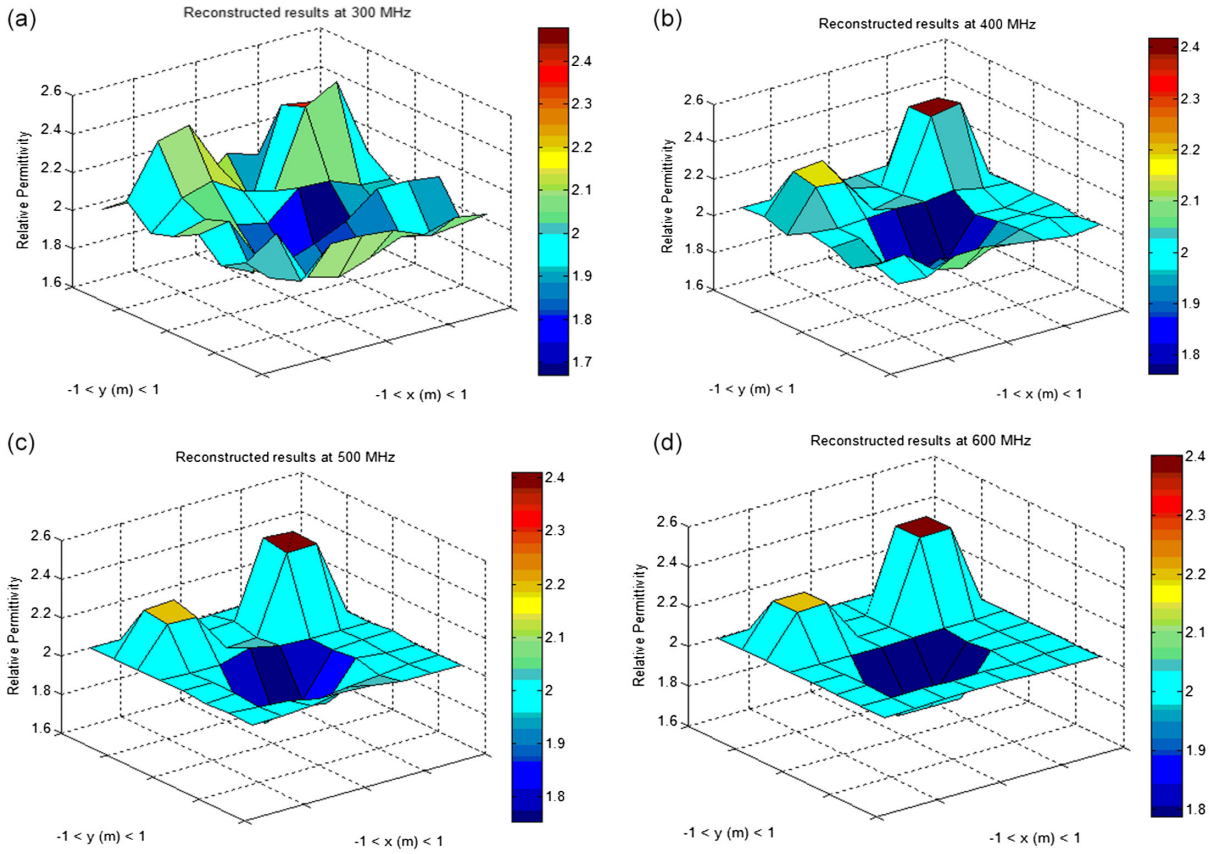

Figure 11

Reconstructed relative permittivity of the buried objects without NR current using the radiating objective function

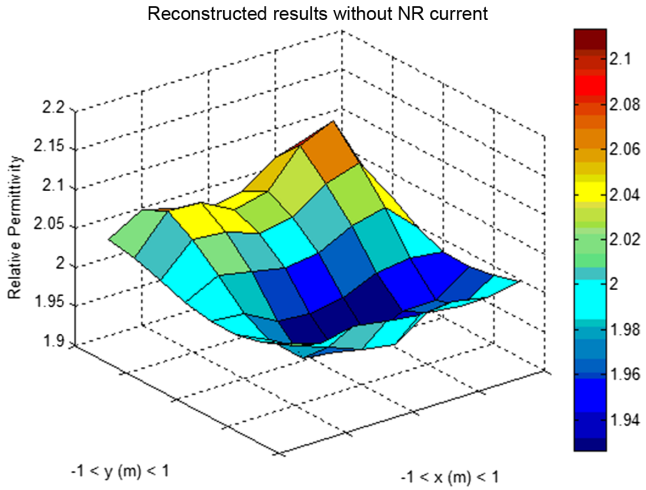

The reconstructed results with and without NR part of currents are shown in Figures 10 and 11, respectively. Due to the single-side incidence, a frequency hopping procedure is utilized to enhance the resolution. From Figures 10 and 11, it can be concluded that the material imaging of the relative permittivity with NR current reconstruction is accurate, while without it, the results are not acceptable. The detection, shape finding, and locating results are satisfactory in both cases.

Table 1
Effect of NR current reconstruction on the imaging of dielectric objects in different background mediums

Medium		Evaluation parameters			
		Detecting	Locating	Shape finding	Material imaging
Free-space	R+NR	+	+	+	+
	Only R	+	+	+	−
Inhomogeneous	R+NR	+	+	+	+
	Only R	+	−	−	−
Stratified	R+NR	+	+	+	+
	Only R	+	+	+	−

In Table 1, the effect of NR current reconstruction on the imaging of dielectric objects located in different background mediums is evaluated. The abbreviations "R+NR" and "only R" in Table 1 represent the cases with and without NR current reconstruction, respectively. The symbol "+" denotes successful results, while "−" indicates a decline in obtaining the desired outcomes.

5. Conclusion

In conclusion, we have successfully applied the SQP-SOM method for inverse scattering of dielectric objects situated in various background mediums. By incorporating NR current reconstruction and separating the radiating and NR subspaces of the induced current space, we have examined its impact on the imaging process. Our findings highlight the significance of NR subspace reconstruction in achieving accurate permittivity profiling of scattering objects. This study contributes to the advancement of imaging techniques for dielectric objects in complex environments. Further research can explore additional enhancements and applications of the SQP-SOM method in solving inverse scattering problems.

Ethical Statement

This study does not contain any studies with human or animal subjects performed by any of the authors.

Conflicts of Interest

The authors declare that they have no conflicts of interest to this work.

Data Availability Statement

Data are available from the corresponding author upon reasonable request.

Author Contribution Statement

Hamidreza Siampour: Conceptualization, Methodology, Software, Validation, Formal analysis, Investigation, Resources, Data curation, Writing – original draft, Writing – review & editing, Visualization, Supervision, Project administration. **Abolghasem Zeidaabadi Nezhad:** Writing – review & editing, Supervision.

References

[1] Xiao, G. (2024). *Electromagnetic sources and electromagnetic fields*. Singapore: Springer.

[2] Awan, F. G., Saleem, O., & Kiran, A. (2019). Recent trends and advances in solving the inverse problem for EEG source localization. *Inverse Problems in Science and Engineering*, *27*(11), 1521–1536. https://doi.org/10.1080/17415977.2018.1490279

[3] Entekhabi, M. N. (2020). Inverse scattering source problems. In F. Bulnes & O. Hachay (Eds.), *Advances in complex analysis and applications* (pp. 27–40). IntechOpen.

[4] Gao, Y., & Zhang, K. (2021). Machine learning based data retrieval for inverse scattering problems with incomplete data. *Journal of Inverse and Ill-Posed Problems*, *29*(2), 249–266. https://doi.org/10.1515/jiip-2019-0101

[5] Ma, W. X. (2020). Inverse scattering for nonlocal reverse-time nonlinear Schrödinger equations. *Applied Mathematics Letters*, *102*, 106161. https://doi.org/10.1016/j.aml.2019.106161

[6] Bevacqua, M. T., Di Meo, S., Crocco, L., Isernia, T., & Pasian, M. (2021). Millimeter-waves breast cancer imaging via inverse scattering techniques. *IEEE Journal of Electromagnetics, RF and Microwaves in Medicine and Biology*, *5*(3), 246–253. https://doi.org/10.1109/JERM.2021.3052096

[7] So, S., Badloe, T., Noh, J., Bravo-Abad, J., & Rho, J. (2020). Deep learning enabled inverse design in nanophotonics. *Nanophotonics*, *9*(5), 1041–1057. https://doi.org/10.1515/nanoph-2019-0474

[8] Ozdemir, C. (2021). *Inverse synthetic aperture radar imaging with MATLAB algorithms*. USA: Wiley.

[9] Song, H., & Kikkawa, T. (2024). Microwave imaging algorithms for breast cancer detection. In A. Miyauchi & H. Kagechika (Eds.), *Biomedical engineering: Imaging systems, electric devices, and medical materials* (pp. 87–107). Jenny Stanford Publishing.

[10] Zhao, P., Lu, C. X., Wang, J., Chen, C., Wang, W., Trigoni, N., & Markham, A. (2019). mID: Tracking and identifying people with millimeter wave radar. In *2019 15th International Conference on Distributed Computing in Sensor Systems,* 33–40. https://doi.org/10.1109/DCOSS.2019.00028

[11] Aldhaeebi, M. A., Alzoubi, K., Almoneef, T. S., Bamatraf, S. M., Attia, H., & Ramahi, O. M. (2020). Review of microwaves techniques for breast cancer detection. *Sensors*, *20*(8), 2390. https://doi.org/10.3390/s20082390

[12] Yao, H., Qin, R., & Chen, X. (2019). Unmanned aerial vehicle for remote sensing applications—A review. *Remote Sensing*, *11*(12), 1443. https://doi.org/10.3390/rs11121443

[13] Withers, P. J., Bouman, C., Carmignato, S., Cnudde, V., Grimaldi, D., Hagen, C. K., . . . , & Stock, S. R. (2021). X-ray computed tomography. *Nature Reviews Methods Primers*, *1*(1), 18. https://doi.org/10.1038/s43586-021-00015-4

[14] Dahlen, F. A., & Tromp, J. (2020). *Theoretical global seismology*. USA: Princeton University Press.

[15] Velásquez, R. M. A., & Lara, J. V. M. (2019). Methodology for failure analysis in shunt reactor by electromagnetic influence caused by high vibration in overload condition. *Engineering Failure Analysis*, *104*, 589–608. https://doi.org/10.1016/j.engfailanal.2019.06.052

[16] Gupta, R., Mitchell, D., Blanche, J., Harper, S., Tang, W., Pancholi, K., . . . , & Flynn, D. (2021). A review of sensing technologies for non-destructive evaluation of structural composite materials. *Journal of Composites Science*, *5*(12), 319. https://doi.org/10.3390/jcs5120319

[17] Ogurtsov, S., Caratelli, D., & Song, Z. (2021). A review of synthesis techniques for phased antenna arrays in wireless communications and remote sensing. *International Journal*

of Antennas and Propagation, *2021*(1), 5514972. https://doi.org/10.1155/2021/5514972

[18] Siampour, H., & Dan, Y. (2016). Si nanowire phototransistors at telecommunication wavelengths by plasmon-enhanced two-photon absorption. *Optics Express*, *24*(5), 4601–4609. https://doi.org/10.1364/OE.24.004601

[19] Siampour, H., Wang, O., Zenin, V. A., Boroviks, S., Siyushev, P., Yang, Y., . . . , & Bozhevolnyi, S. I. (2020). Ultrabright single-photon emission from germanium-vacancy zero-phonon lines: Deterministic emitter-waveguide interfacing at plasmonic hot spots. *Nanophotonics*, *9*(4), 953–962. https://doi.org/10.1515/nanoph-2020-0036

[20] Goel, S., Leedumrongwatthanakun, S., Valencia, N. H., McCutcheon, W., Tavakoli, A., Conti, C., . . . , & Malik, M. (2024). Inverse design of high-dimensional quantum optical circuits in a complex medium. *Nature Physics*, *20*, 232–239.

[21] Siampour, H., O' Rourke, C., Brash, A. J., Makhonin, M. N., Dost, R., Hallett, D. J., . . . , & Fox, A. M. (2023). Observation of large spontaneous emission rate enhancement of quantum dots in a broken-symmetry slow-light waveguide. *npj Quantum Information*, *9*(1), 15. https://doi.org/10.1038/s41534-023-00686-9

[22] Dory, C., Vercruysse, D., Yang, K. Y., Sapra, N. V., Rugar, A. E., Sun, S., . . . , & Vučković, J. (2019). Inverse-designed diamond photonics. *Nature Communications*, *10*(1), 3309. https://doi.org/10.1038/s41467-019-11343-1

[23] Cakoni, F., Colton, D., & Haddar, H. (2022). *Inverse scattering theory and transmission eigenvalues*. USA: Society for Industrial and Applied Mathematics.

[24] Harris, I. (2023). Regularized factorization method for a perturbed positive compact operator applied to inverse scattering. *Inverse Problems*, *39*(11), 115007. https://doi.org/10.1088/1361-6420/acfd59

[25] Liu, S., Baniamerian, J., & Fedi, M. (2020). Imaging methods versus inverse methods: An option or an alternative? *IEEE Transactions on Geoscience and Remote Sensing*, *58*(5), 3484–3494. https://doi.org/10.1109/TGRS.2019.2957412

[26] Bertero, M., Boccacci, P., & de Mol, C. (2021). *Introduction to inverse problems in imaging*. USA: CRC Press.

[27] Lucka, F., Pérez-Liva, M., Treeby, B. E., & Cox, B. T. (2022). High resolution 3D ultrasonic breast imaging by time-domain full waveform inversion. *Inverse Problems*, *38*(2), 025008. https://doi.org/10.1088/1361-6420/ac3b64

[28] Chen, X. (2010). Subspace-based optimization method for solving inverse-scattering problems. *IEEE Transactions on Geoscience and Remote Sensing*, *48*(1), 42–49. https://doi.org/10.1109/TGRS.2009.2025122

[29] Yin, T., Wei, Z., & Chen, X. (2020). Non-iterative methods based on singular value decomposition for inverse scattering problems. *IEEE Transactions on Antennas and Propagation*, *68*(6), 4764–4773. https://doi.org/10.1109/TAP.2020.2969708

[30] Ye, N., Roosta-Khorasani, F., & Cui, T. (2019). Optimization methods for inverse problems. In D. R. Wood, J. de Gier, C. E. Praeger & T. Tao (Eds.), *2017 MATRIX annals* (pp. 121–140). Springer. https://doi.org/10.1007/978-3-030-04161-8_9

[31] Brown, T., Narendra, C., Vahabzadeh, Y., Caloz, C., & Mojabi, P. (2020). On the use of electromagnetic inversion for metasurface design. *IEEE Transactions on Antennas and Propagation*, *68*(3), 1812–1824. https://doi.org/10.1109/TAP.2019.2944544

[32] Devaney, A. J., & Wolf, E. (1973). Radiating and nonradiating classical current distributions and the fields they generate. *Physical Review D*, *8*(4), 1044. https://doi.org/10.1103/PhysRevD.8.1044

[33] Costanzo, S., Flores, A., & Buonanno, G. (2022). Machine learning approach to quadratic programming-based microwave imaging for breast cancer detection. *Sensors*, *22*(11), 4122. https://doi.org/10.3390/s22114122

[34] Fu, Z., Liu, G., & Guo, L. (2019). Sequential quadratic programming method for nonlinear least squares estimation and its application. *Mathematical Problems in Engineering*, *2019*(1), 3087949. https://doi.org/10.1155/2019/3087949

[35] Chen, X. (2010). Subspace-based optimization method for inverse scattering problems with an inhomogeneous background medium. *Inverse Problems*, *26*(7), 074007. https://doi.org/10.1088/0266-5611/26/7/074007

[36] Volakis, J. L., Chatterjee, A., & Kempel, L. C. (1998). *Finite element method electromagnetics: Antennas, microwave circuits, and scattering applications*. USA: Wiley.

[37] Kong, J. A. (2005). *Electromagnetic wave theory*. UK: EMW Pub.

[38] Cui, T. J., Wiesbeck, W., & Herschlein, A. (1998). Electromagnetic scattering by multiple three-dimensional scatterers buried under multilayered media. I. Theory. *IEEE Transactions on Geoscience and Remote Sensing*, *36*(2), 526–534. https://doi.org/10.1109/36.662735

[39] Nisar, K. S., Ilhan, O. A., Abdulazeez, S. T., Manafian, J., Mohammed, S. A., & Osman, M. S. (2021). Novel multiple soliton solutions for some nonlinear PDEs via multiple Exp-function method. *Results in Physics*, *21*, 103769. https://doi.org/10.1016/j.rinp.2020.103769

[40] Sun, Z. B., Sun, Y. Y., Li, Y., & Liu, K. P. (2019). A new trust region–sequential quadratic programming approach for nonlinear systems based on nonlinear model predictive control. *Engineering Optimization*, *51*(6), 1071–1096. https://doi.org/10.1080/0305215X.2018.1509960

[41] Yang, C., Wang, M., Wang, W., Pu, Z., & Ma, M. (2021). An efficient vehicle-following predictive energy management strategy for PHEV based on improved sequential quadratic programming algorithm. *Energy*, *219*, 119595. https://doi.org/10.1016/j.energy.2020.119595

How to Cite: Siampour, H., & Nezhad, A. Z. (2024). Revealing the Invisible: Imaging Through Non-radiating Subspace. *Journal of Optics and Photonics Research*, *1*(4), 159–169. https://doi.org/10.47852/bonviewJOPR42022785